Advanced Intelligent Discovery

ADVANCED INTELLIGENT DISCOVERY Open Access

RESEARCH ARTICLE OPEN ACCESS

Evaluating Three Foundation Potentials for Predicting Selected Properties of the Co–Ni–Ru Alloy System

Subah Mubassira[1] | Thu Nguyen[1] | Anvesh Nathani[1] | Shoutian Sun[2] | Ming Hu[3] | Yanqing Su[1] | Bin Wang[2,4] | Iman Ghamarian[1] | Shuozhi Xu[1]

[1]School of Aerospace and Mechanical Engineering, University of Oklahoma, Norman, Oklahoma, USA | [2]School of Sustainable Chemical, Biological and Materials Engineering, University of Oklahoma, Norman, Oklahoma, USA | [3]Department of Mechanical Engineering, University of South Carolina, Columbia, South Carolina, USA | [4]Department of Chemical and Biological Engineering, Tufts University, Medford, Massachusetts, USA

Correspondence: Shuozhi Xu (shuozhixu@ou.edu)

Received: 30 October 2025 | **Revised:** 17 February 2026 | **Accepted:** 15 May 2026

Keywords: elastic constant | foundation potential | lattice parameter | multi-principal element alloy | stacking fault energy

ABSTRACT

This study evaluates the efficacy of three foundation potentials (FPs)—SevenNet, DPA, and Orb—in predicting selected properties of several alloys and metals that are based on three elements: Co, Ni, and Ru. The analyzed systems comprise the face-centered cubic (FCC) structured CoNiRu, Co_2Ni_2Ru, and pure Ni, as well as hexagonal close-packed (HCP) structured CoNiRu and $CoNiRu_2$. Properties include lattice parameters, elastic constants, and generalized stacking fault energies (GSFEs), assessed at 0 and/or 300 K. Results are compared against density functional theory (DFT) data whenever available. We found that all FPs typically forecast lattice parameters within 2.5% of DFT values at 0 K. At 300 K; both DPA and SevenNet largely successfully capture the expected thermal expansion trend. Orb was excluded at 300 K due to lattice instability. For elastic constants, DPA consistently captures thermal softening at elevated temperatures, while Orb and SevenNet exhibit potential-dependent discrepancies. For GSFEs, DPA exhibits the closest alignment with DFT in both FCC and HCP structures, while Orb consistently shows the poorest performance. By elucidating the respective strengths and limitations of FPs, our findings offer insights into the robustness of these interatomic potentials for high-throughput screening and predictive modeling of alloys.

1 | Introduction

In the past two decades, multiprincipal element alloys (MPEAs) have gained great attention as promising materials for extreme environments, with potential applications in aerospace propulsion, gas turbines, nuclear energy systems, thermal protection components, and high-temperature chemical processing equipment [1]. Distinguished by the absence of a single dominant elemental species, MPEAs are made up of three or more principal elements that are dispersed randomly or near randomly throughout a crystalline lattice [2]. Local compositional fluctuations and noticeable lattice distortions are two features of MPEAs at the atomic scale [3]. MPEAs have distinct deformation mechanisms, microstructures, and physical characteristics that distinguish them from the typical behavior of their constituent pure elements, according to both experimental studies [2, 4–7] and atomistic simulations [8–10]. Notably, some MPEA compositions exhibit remarkable combinations of mechanical properties that are uncommon in conventional materials, such as simultaneously increased yield strength and ductility [5].

The FCC CoCrFeMnNi MPEA—commonly known as the Cantor alloy [2]—remains one of the most extensively studied MPEAs. It exhibits excellent ductility and strong strain-hardening capabilities, though its yield strength at room temperature remains modest [11, 12]. These findings have driven ongoing research aimed at enhancing mechanical performance through targeted alloy design. This includes optimizing composition, tuning microstructures and

nanostructures, promoting precipitation strengthening, and evaluating the effects of grain size and operating temperature on yield strength [13–17]. Wu et al. [18] demonstrated, through a systematic study of phase stability and mechanical behavior in equiatomic binary, ternary, and quaternary subsets of the CoCrFeMnNi system, that certain alloys, such as CoCrNi and CoCrFeNi, outperform the full five-component alloy in terms of strength at room temperature. At cryogenic temperatures, these alloys exhibit enhanced mechanical performance due to the activation of twinning-induced plasticity, a mechanism facilitated by the reduction in intrinsic stacking fault energy (ISFE) with decreasing temperature [19]. Notably, CoCrNi exhibits a lower ISFE (18–22 mJ/m^2 [20, 21]) compared with CoCrFeMnNi (27–30 mJ/m^2 [20, 22]), which promotes the development of a dense network of nanotwins and enables transformation-induced plasticity under high strain conditions [23].

Despite these insights, much of the existing research has remained focused on modifying the elemental ratios within the CoCrFeMnNi system, with limited exploration of alternative elements. Motivated by the exceptional performance of CoCrNi and the central role of lattice friction in strengthening mechanisms for MPEAs [2, 24], Charpagne et al. [25] investigated Co_2Ni_2Ru, showing that its low ISFE enables twinning-induced plasticity and its high lattice friction promotes early twinning and dense planar defects, leading to enhanced work hardening. Ru was selected due to several advantageous attributes. While several HCP elements could potentially tune the ISFE in this system, Ru stands out due to its significantly larger atomic radius than both Co and Ni, contributing to enhanced lattice friction, which is a key strengthening mechanism in MPEAs, as well as a high shear modulus of 173 GPa, substantially higher than that of Cr (115 GPa [26]). The same experimental study also found that the equimolar CoNiRu is an FCC/HCP dual-phase alloy. On the modeling side, Su et al. [27] focused on the FCC phase of the CoNiRu alloy, reporting stacking fault widths of screw and edge dislocations using a density functional theory (DFT)-informed phase-field model. Although this study provided important atomistic insights, its scope was limited to the equimolar composition and the FCC phase only.

Exploring additional compositions and phases systematically is hindered by the complexity and high cost of experiments. Atomistic simulations provide a powerful means to bridge this gap, offering direct insights into defect energetics, lattice stability, and deformation mechanisms. The primary component of atomistic simulations is the interatomic potential, which defines the potential energy surfaces (PES) of atomic interactions within a material system. In recent years, the emergence of machine learning (ML) has introduced transformative possibilities for developing interatomic potentials [28–31]. These models now offer energy and force predictions with accuracy comparable to that of DFT, while operating at a fraction of the computational cost. This significant efficiency gain has enabled machine learning-based interatomic potentials (MLIPs) to accelerate—and in some cases, replace—conventional DFT calculations, opening new possibilities for the rapid, in silico discovery and design of complex materials [32].

The concept of MLIPs was first introduced by Blank et al. [33] in 1995, who developed a neural network framework for predicting the PES. Later, in 2010, Bartók et al. [34] proposed the Gaussian approximation potential (GAP) for modeling diamond. Unlike traditional potentials, GAP does not rely on a predefined functional form, making it well-suited for capturing complex and high-dimensional energy landscapes. As systems grew more complex and the need for scalable solutions increased, models like SchNet [35] and subsequently PhysNet [36] were introduced. The progress in training MLIPs has been significantly enhanced by decades of accumulated DFT calculations and the emergence of extensive open-access materials databases. Notable examples include the Materials Project [37], Open Quantum Materials Database [38], AFLOWlib [39], Alexandria [40], and NOMAD [41]. These repositories offer a broad spectrum of data covering materials composed of nearly all elements and exhibiting diverse crystal structures.

Traditionally, MLIPs were tailored to specific chemical systems, restricting their transferability to elements that were not involved during training. This landscape began to shift in 2022 with the introduction of an MLIP for materials based on graph neural networks with three-body interactions (M3GNet) for 89 elements in the periodic table [42]. This advancement marked the rise of foundation potentials (FPs)—also known as the universal MLIPs—a new class of models engineered to handle a broad spectrum of chemistry and crystal structures with minimal system-specific customization. Hajibabaei and Kim [43] demonstrated the applicability of FPs in modeling solid electrolytes, in which Li diffusivity across diverse ternary and quaternary crystal systems was explored. Recently, Loew et al. benchmarked seven state-of-the-art FPs—M3GNet, CHGNet, MACE-MP-0, SevenNet-0, MatterSim-v1, Orb, and eqV2-M—evaluating their performance in predicting phonon-related properties across diverse materials systems [44]. Huang et al. [45] investigated transfer learning within the CHGNet FP framework to improve accuracy across fidelity levels. Their work highlights that proper energy referencing and multifidelity learning are essential for achieving reliable cross-functional transferability in next-generation FPs.

Jakob et al. [46] evaluated the applicability of general-purpose FPs such as M3GNet and MACE for structure prediction by considering the merits and flaws of these FPs for structural prediction, particularly for end-to-end workflows beyond energy or force prediction. Yu et al. [47] considered four graph-based FPs in a manner that allowed for systematic evaluation and emphasized cross-material transferability but omitted phase-sensitive or defect-level accuracy tests. Focassio et al. [48] have shown that pretrained models such as CHGNet, M3GNet, and MACE frequently lack generalization in usability to surface or defect environments, due to a lack of appropriate coverage of out-of-domain in training data. Casillas–Trujillo et al. [49] found similar limitations in predicting subtle energetic differences, such as mixing enthalpies and volumes in binary alloys. Moreover, Deng et al. [50] identified a systematic softening of the PES in M3GNet, CHGNet, and MACE-MP-0 that was rooted in systematically underpredicted curvatures from biased near-equilibrium training data, which led to systematically low predictions of energies and forces across high-energy configurations such as defects and solid solution. Most existing validations of FPs focus broadly on their predictive performance across a vast chemical landscape,

typically assessing their accuracy in reproducing global energy and structural trends over diverse material classes.

However, such broad-spectrum assessments often overlook critical nuances—specifically, they do not rigorously test whether these potentials can reliably capture the defect-sensitive properties essential for modeling complex alloy systems—leaving a gap as to whether the claimed universality of FPs meaningfully extends to the fine-scale structural and mechanical descriptors that dictate alloy deformation. Our study addresses this important gap by rigorously examining whether state-of-the-art FPs —deep potential with attention (DPA) [51], SevenNet [52], Orb [53]—can reliably predict properties of the chemically complex Co–Ni–Ru system. Three FPs are chosen because they span the two dominant MLIP paradigms [54]: descriptor-based local networks (DPA) versus SE(3)-equivariant graph message passing (SevenNet and Orb). We include both SevenNet and Orb to probe inductive-bias differences within the equivariant family. SevenNet, derived from NequIP, adds parallelized message passing while retaining NequIP's data efficiency, accuracy, and equivariant representations [55]. Orb couples smooth overlap of atomic positions descriptors with a graph-based simulation engine, providing a flexible and robust framework for complex atomic interactions [56]. All three FPs provide mature open-source stacks and public foundation checkpoints that cover our target element set.

In this study, we benchmark these three FPs to compute basic structural parameters, including lattice parameters and elastic constants, as well as generalized SFE (GSFEs) for selected compositions at 0 and/or 300 K. The systems studied include FCC and HCP structures: CoNiRu (FCC), Co_2Ni_2Ru (FCC), CoNiRu (HCP), and $CoNiRu_2$ (HCP), as well as pure Ni (FCC) as a reference system. The selections of $CoNiRu_2$ and Co_2Ni_2Ru are supported by available experimental evidence [25]. Although CoNiRu is not experimentally observed as a single-phase material and thus does not possess direct practical relevance, both FCC and HCP configurations were examined here due to their potential theoretical relevance. By applying these FPs to structurally distinct configurations, we aim to assess their consistency and transferability across different phases and chemistries. Where available, DFT results are used as benchmarks to evaluate the performance of the FPs. This study does not attempt to rank or definitively validate the potentials, but rather presents a comparative dataset that can inform future modeling efforts and guide the selection of FPs based on specific structure and composition.

We emphasize that this work focuses exclusively on chemically random alloys; that is, neither chemical short-range ordering (CSRO) nor site-preferential ordering is considered. That said, numerous atomistic studies have demonstrated that CSRO can affect structural and mechanical properties in MPEAs such as CoCrNi [57, 58] and MoNbTa [59]. In particular, CSRO has been shown to modify dislocation dynamics in MoNbTaW [60], increase stacking fault energies in MoNbTi and TaNbTi alloys [61], and enhance fracture toughness in CoCrNi [62]. In parallel, several studies have investigated the influence of sublattice site-occupancy behavior on the properties of MPEAs [63–65]. For example, Zhang et al. [66] showed that incorporating site preference via site-occupying fraction-based ordered configurations markedly modifies thermodynamic and mechanical properties, leading to lower energies, enhanced stability, and substantially higher elastic moduli and hardness compared with random structures. Similarly, Chen et al. [67] reported for FCC CoNiV and CoCrNi MPEAs that accounting for site preference significantly alters atomic distributions, reduces configurational entropy, modifies lattice distortion by 11%, and changes clustering characteristics relative to random-alloy assumptions.

2 | Methodology

2.1 | Atomistic Simulations

Atomistic simulations are performed using LAMMPS [68]. All initial atomistic structures are generated using Atomsk [69]. Table 1 summarizes the simulated materials, crystal structures, temperatures, and FPs employed in this study.

2.1.1 | SevenNet

The SevenNet-0 potential [70] was employed in this study. SevenNet is a framework based on a graph neural network (GNN) architecture that predicts atomic energies and pressures by representing atomic structures as graphs and learning interatomic interactions through message-passing operations. This flexible architecture eliminates the need for manual feature engineering by learning hierarchical atomic representations directly from raw atomic numbers and positions. As a result, SevenNet can effectively model chemically diverse systems with high accuracy and transferability, making it well-suited for simulating a broad range of materials systems [52].

GNN-IPs predict total energy and atomic forces using atomic numbers and atomic positions. In the embedding layer, atomic numbers initialize the node features $h^{(1)}$. Atoms are connected by edges if they are within a predefined cutoff distance r_c. Each edge feature e_{vw} encodes the distance and unit displacement vector between atoms v and w. Node and edge features are generally treated as tensors.

The GNN architecture consists of a stack of message-passing layers. Each message-passing layer updates node features by aggregating messages from neighboring nodes and edges. Following the final message-passing layer, a readout layer predicts atomic energies based on the final node representations. Across a total of T message-passing layers, each layer t contains

TABLE 1 | Summary of simulated materials, crystal structures, temperatures, and FPs used. Note that GSFEs are only calculated at 0 K.

Alloys	Structures	Temperature	FPs
CoNiRu	FCC and HCP	0 and 300 K	SevenNet, DPA, and Orb
Co_2Ni_2Ru	FCC		
$CoNiRu_2$	HCP		
Pure Ni	FCC		

two trainable functions: a message function M_t and an update function U_t [71]:

$$m_v^{(t+1)} = \sum_{w \in \mathcal{N}(v)} M_t(h_v^{(t)}, h_w^{(t)}, e_{vw}) \tag{1}$$

$$h_v^{(t+1)} = U_t(h_v^{(t)}, m_v^{(t+1)}) \tag{2}$$

where $t = 1, 2, \ldots, T$, $\mathcal{N}(v)$ is the neighbor set of node v, and $m_v^{(t+1)}$ is the message gathered from $\mathcal{N}(v)$. The propagation of node features across connected edges in each message-passing layer is governed by the functions M_t and U_t. With every additional message-passing layer, the receptive field of GNN-based interatomic potentials expands, as nodes iteratively incorporate information from their neighboring atoms.

The total potential energy (E) of a system can be represented as the summation of individual atomic contributions, while the atomic forces are obtained from the negative gradient of the energy:

$$E = \sum_{i=1}^{N} E_i \tag{3}$$

$$F_i = -\nabla_{\mathbf{r}_i} E \tag{4}$$

where E_i and F_i denote the atomic energy and force associated with atom i, respectively. The symbol N represents the total number of atoms in the simulation cell, and ∇_i is the gradient operator with respect to the position vector $\mathbf{r}_i$.

2.1.2 | DPA

We use in this study the DPA-2 [51] model that was implemented in the DeePMD-kit v3 [72], which is a package for constructing MLIPs with near first-principles accuracy and atomistic efficiency. It employs deep neural networks trained on reference datasets, typically generated from DFT calculations, to represent the PES and atomic forces. In the DPA framework, the energy of an N-atom system and the force on individual atoms are represented by Equations (3) and (4).

The DPA model was developed to predict the atomic energy contribution (E_i) based on $\mathbf{z}$ and $\mathbf{r}$:

$$E_i = \mathcal{F}(\mathcal{D}_i(\mathbf{r}, \mathbf{z})) \tag{5}$$

where $\mathcal{D}_i$ indicates the descriptor of atom i, The descriptor is a smooth mapping from atomic numbers and coordinates to a hidden representation invariant to translation, rotation, and permutation. The atomic numbers are represented by the set $\mathbf{z} = (z_1, z_2, \ldots, z_i, \ldots, z_N)$, and their corresponding atomic positions are denoted by $\mathbf{r} = (r_1, r_2, \ldots, r_i, \ldots, r_N)$. The fitting network $\mathcal{F}$ is modeled by a standard multiple-layer perceptron (MLP) composed of an energy-biasing layer:

$$\mathcal{F}(\mathcal{D}_i) = e_{\text{bias}}(\text{MLP}(\mathcal{D}_i)) \tag{6}$$

The energy bias layer (e_{bias}) adds a constant bias to the atomic energy. In practical applications, the energy bias is determined by a least-squares fitting of energies in the training data. $\mathcal{D}_i$ is expressed as

$$\mathcal{D}_i = \text{concat}(f_i^0, f_i^2) \tag{7}$$

where f_i^0 and f_i^2 denote the single-atom representations of atom i. The representation of f_i^0 is defined as:

$$f_i^0 = \text{MLP}(\text{one\_hot}(z_i)) \tag{8}$$

where the atomic number z_i is converted into a one-hot representation and embedded by an MLP. Then, the single-atom representation is updated by the reprint (representation-initializer) layer that encodes the information of local configuration, which is expressed by pair-atom representation g_{ij}^0 and h_{ij}^0:

$$f_i^1 = \text{repinit}(f_i^0, g_{ij}^0, h_{ij}^0) \tag{9}$$

In the meantime, f_i^2 is mapped from single-atom representation and pair-atoms representations g_{ij}^0 and h_{ij}^0 with a multiple-layer structure:

$$f_i^2 = \text{repformer} \circ \ldots \circ \text{repformer}\Big(\text{linear}(f_i^1), \text{linear}(g_{ij}^1), h_{ij}^1\Big) \tag{10}$$

where the single and pair-atom representations are updated by repformer layers that are stacked 12 times. The "$\circ$" in the equation above denotes the layer composition.

g_{ij}^0 and h_{ij}^0 are defined as:

$$g_{ij}^0 = s(r_{ij}) \tag{11}$$

$$h_{ij}^0 = s(r_{ij}) \times \left(\frac{x_{ij}}{|r_{ij}|}, \frac{y_{ij}}{|r_{ij}|}, \frac{z_{ij}}{|r_{ij}|}\right) \tag{12}$$

where $s(r_{ij})$ is the switched inverse distance function:

$$s(r_{ij}) = \frac{w_{ij}}{|r_{ij}|}, \quad w_{ij} = w(|r_{ij}|) \tag{13}$$

The switch function w is provided as:

$$w(|r_{ij}|) = \begin{cases} 1 & \text{if } r_{ij} < r_{\text{cs}} \\ u^3(-6u^2 + 15u - 10) + 1 & \text{if } r_{\text{cs}} \le r_{ij} < r_c \\ 0 & \text{if } r_c \le r_{ij} \end{cases}$$

where r_c is the cut-off radius, $u = (|r_{ij}| - r_{\text{cs}})/(r_c - r_{\text{cs}})$ and $r_{\text{cs}} < r_c$ is the starting point of the smooth switch. The presentations of g_{ij}^1 and h_{ij}^1 are established in the same way as g_{ij}^0 and h_{ij}^0, with the only potential variation being the selection of the cut-off radius r_c.

2.1.3 | Orb

Orb is built on a graph network simulator backbone with smoothed graph attention. In this study, we use Orb-v2 [53]. Atomic configurations are represented as a periodic, cutoff graph:

$$\mathcal{G} = (\mathcal{V}, \mathcal{E}, C)$$

where nodes $i \in \mathcal{V}$ represent atoms (embedded from species only, without absolute positions to preserve translational invariance) and directed edges $(i \to j) \in \mathcal{E}$ connect neighbors within a periodic

boundary condition (PBC)-aware cutoff radius r_c, determined by the optional unit cell $C \in \mathbb{R}^{3\times3}$.

Edge features are constructed from the interatomic distance $\mathbf{r}_{ij} = \mathbf{r}_j - \mathbf{r}_i$ and its radial basis expansion:

$$\begin{aligned} e_{ij} &= \left[r_{ij}, \hat{\mathbf{r}}_{ij}, \mathrm{RBF}(r_{ij})\right], \\ \mathrm{RBF}_\ell(x) &= \exp\left(-\frac{(x-\mu_\ell)^2}{\sigma_\ell^2}\right), \quad \ell = 1, \ldots, p \end{aligned} \tag{14}$$

where $r_{ij} = |\mathbf{r}_{ij}|$ and $\hat{\mathbf{r}}_{ij} = \mathbf{r}_{ij}/r_{ij}$ and RBF stands for radial basis function.

The message-passing core, known as the processor in Orb, is composed of T stacked message-passing layers, which update node embeddings using attention-weighted, distance-smoothed messages:

$$\begin{aligned} m_i^{(t)} &= \sum_{j\in\mathcal{N}(i)} \alpha_{ij}^{(t)}\, \phi_e^{(t)}\left(e_{ij}, h_i^{(t)}, h_j^{(t)}\right), \\ h_i^{(t+1)} &= h_i^{(t)} + \phi_v^{(t)}\left(h_i^{(t)}, m_i^{(t)}\right) \end{aligned} \tag{15}$$

where t is the layer index, $h_i^{(t)}$ the node (atom) embedding at layer t, and $\phi_e^{(t)}$ and $\phi_v^{(t)}$ are learnable update functions. The attention gates are defined as

$$\alpha_{ij}^{(t)} = \sigma\left(\mathbf{w}^{(t)\top}\phi_a^{(t)}(e_{ij})\right) \underbrace{\left(1 - (r_{ij}/r_{\max})^p\right)_+}_{\mathrm{cutoff}(r_{ij})} \tag{16}$$

where $\sigma(\cdot)$ is the logistic function and $(\cdot)_+ = \max(\cdot, 0)$. The multiplicative cutoff guarantees continuity and locality near the cutoff distance.

The decoder, which is the readout module that maps the final node embeddings $h_i^{(T)}$ from the processor to physical outputs, produces global energy, per-atom forces, and stress through lightweight MLP heads:

$$E = \phi_E\left(\frac{1}{N}\sum_i h_i^{(T)}\right), \qquad \mathbf{f}_i = \phi_F\left(h_i^{(T)}\right), \qquad \boldsymbol{\sigma} = \phi_\sigma\left(\frac{1}{N}\sum_i h_i^{(T)}\right) \tag{17}$$

Unlike conservative MLIPs, Orb does not compute forces as gradients of the energy but predicts them directly in one forward pass. To ensure physical consistency, corrections are applied: First, the net force is removed:

$$\hat{\mathbf{f}}_i = \mathbf{f}_i - \frac{1}{N}\sum_{j=1}^{N} \mathbf{f}_j \tag{18}$$

and for non-periodic systems, a minimal-norm correction $\delta\mathbf{f}_i$ is added to enforce zero net torque:

$$\begin{aligned} &\tilde{\mathbf{f}}_i = \hat{\mathbf{f}}_i + \delta\mathbf{f}_i, \\ &\delta\mathbf{f} = \arg\min_{\{\delta\mathbf{f}_i\}} \sum_i \|\delta\mathbf{f}_i\|^2 \ \text{ subject to } \ \sum_i \delta\mathbf{f}_i = 0, \\ &\sum_i \mathbf{r}_i \times \delta\mathbf{f}_i = -\sum_i \mathbf{r}_i \times \hat{\mathbf{f}}_i \end{aligned} \tag{19}$$

This architecture combines local distance-based smoothing with attention-driven anisotropy, producing a transferable MLIP that is continuous, translationally invariant, and efficient for large-scale simulations.

2.2 | DFT Calculations

We use DFT calculation data as benchmark for our FP calculations. Table 2 summarizes existing DFT data utilized in this study, all of which were performed at 0 K.

For a better benchmark, we have performed new DFT calculations at 0 K in this work. Our new DFT data include the lattice parameters and elastic constants of HCP CoNiRu, HCP $CoNiRu_2$, and FCC Co_2Ni_2Ru, as well as the ISFE of FCC Co_2Ni_2Ru. All DFT simulations were carried out using VASP [74, 75]. All calculations were performed under constant-pressure conditions, allowing simultaneous relaxation of the atomic positions, lattice parameters, and cell volume. The Methfessel–Paxton smearing scheme [76] with a width of 0.05 eV was applied to handle partial occupancies. A plane-wave energy cutoff of 551.98 eV was used for the basis set, and the Brillouin zone was sampled using an 11 × 11 × 11 Monkhorst–Pack k-point grid [77]. Exchange-correlation interactions were described within the generalized gradient approximation using the Perdew–Burke–Ernzerhof functional [78]. Projector-augmented wave pseudopotentials [79, 80] distributed with VASP version 6.4.3 were employed for all elements. Electronic self-consistency was achieved when the total energy difference between successive iterations was smaller than 10^{-4} eV/atom, and ionic relaxation was performed until the largest residual force on any atom was below 10^{-3} eV Å^{-1}. Upon full relaxation, the resulting configurations were well-converged and structurally stable, with no evidence of long-range atomic distortions.

2.3 | Basic Structural Parameters

We have calculated the lattice parameters and elastic constants at 0 and 300 K.

At 0 K, a relaxation-based approach was used to determine the lattice parameter of each material. The process begins by constructing a unit cell with an initial lattice parameter, and then the cell is relaxed under the condition that all three normal stress components reach zero. Finally, the equilibrium lattice parameter, a_0, is calculated from the volume of the fully relaxed unit cell [81]. At 300 K, the pre-relaxed 0 K structures were used as initial configurations. Each system was equilibrated under isothermal–isobaric (NPT) conditions, allowing both atomic positions and cell dimensions

TABLE 2 | Existing DFT data for FCC CoNiRu and pure Ni.

Alloy	Lattice parameter, Å	Elastic constants, GPa	GSFE, mJ/m^2
FCC CoNiRu [27]	a_0 = 3.624	$C_{11}^* = 404.43$, $C_{12}^* = 165.85$, $C_{44}^* = 147.03$	USFE = 376.41 ISFE = 44.56
Pure Ni [73]	a_0 = 3.519	$C_{11}^* = 278.87$, $C_{12}^* = 158.83$, $C_{44}^* = 132.18$	USFE = 289 ISFE = 144.50

to relax simultaneously. After achieving thermal equilibrium, the time-averaged cell dimensions were extracted from the simulation outputs to determine the equilibrium lattice parameter. The obtained values inherently account for the effects of thermal expansion at 300 K [59].

At 0 K, the stiffness tensor **C** is obtained using the stress–strain method to evaluate the elastic constants [82]. At 300 K, the Born-matrix method was used to calculate the elastic constants [83].

At each temperature, the effective elastic constants for FCC materials are calculated by:

$$C_{11}^{*} = \frac{C_{11} + C_{22} + C_{33}}{3} \tag{20}$$

$$C_{12}^{*} = \frac{C_{12} + C_{13} + C_{23}}{3} \tag{21}$$

$$C_{44}^{*} = \frac{C_{44} + C_{55} + C_{66}}{3} \tag{22}$$

In the meantime, the effective elastic constants for HCP materials are calculated by:

$$C_{11}^{*} = \frac{C_{11} + C_{12}}{2} \tag{23}$$

$$C_{12}^{*} = C_{12} \tag{24}$$

$$C_{13}^{*} = \frac{C_{13} + C_{23}}{2} \tag{25}$$

$$C_{33}^{*} = C_{33} \tag{26}$$

$$C_{44}^{*} = \frac{C_{44} + C_{55}}{2} \tag{27}$$

2.4 | GSFE

All GSFE calculations were performed at 0 K. For slips on {111} planes in FCC crystals and those on basal planes in HCP materials, ISFE is identified as a local minimum on the GSFE curve, while the unstable SFE (USFE) the smaller local maximum [73, 84, 85].

In this study, GSFE curves are generated by rigidly displacing the upper half of the simulation cell relative to the lower half in a specified crystallographic direction within a given slip plane. Displacements are applied incrementally over one periodic unit length, equivalent to the magnitude of the Burgers vector b for a full dislocation. Within a given alloy, the GSFE curve can vary between different parallel slip planes due to fluctuations in the local atomic environment [86–88]. To ensure statistical reliability, we compute GSFE curves on at least 10 different slip planes for each MPEA system [27, 59].

3 | Results and Discussion

3.1 | Lattice Parameter

Figure 1 presents the calculated lattice parameters for the FCC and HCP systems at 0 and 300 K using three FPs. For each HCP alloy, we have presented two lattice parameters, including the hexagonal base length a_0 and the height of the conventional unit cell c; for each FCC material, only a_0 is presented. As discussed in Section 2.2, DFT reference data are available only at 0 K. Overall, all three FPs predict FCC and HCP lattice parameters with good fidelity. At 0 K, errors with respect to DFT are consistently below 2.5%, with Orb performing best for HCP systems and DPA providing the most consistent description of FCC materials. At 300 K, both DPA and SevenNet reproduce the expected thermal trends, although subtle potential-dependent differences are evident in the HCP phases.

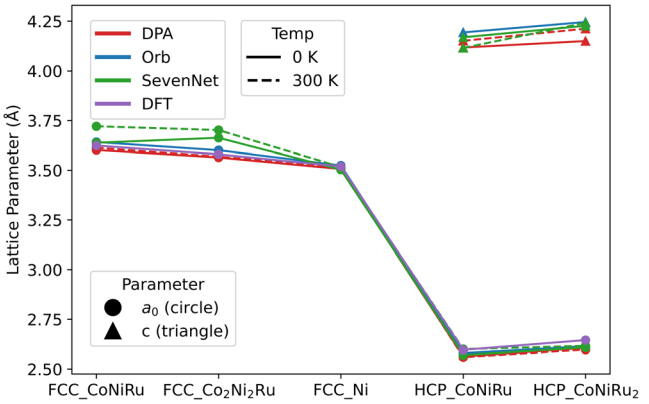

FIGURE 1 | Calculated lattice parameters of FCC alloys, HCP alloys, and pure Ni at 0 and 300 K.

3.1.1 | FCC Materials

Using SevenNet, a_0 for FCC CoNiRu and pure Ni were calculated using cells including 6,750 atoms at both 0 and 300 K. For Co_2Ni_2Ru, a larger cell including 11,664 atoms was utilized. On the other hand, DPA and Orb simulations employed uniformly larger cells, including 20,328 atoms for FCC structured CoNiRu, Co_2Ni_2Ru, and pure Ni at both temperatures. All simulations for HCP-structured CoNiRu and $CoNiRu_2$ were performed using cells comprising 20,800 atoms, irrespective of the FP employed.

For the FCC alloys at 0 K, all three FPs reproduce the DFT lattice parameters within ≈ 2.5%. In FCC CoNiRu, the smallest deviation from the DFT value ($a_0 = 3.624$ Å [27]) was obtained using SevenNet, which overestimates a_0 by 0.38%. DPA and Orb yielded errors of −0.62% and +0.49%, respectively. At 0 K, our DFT calculation for FCC-structured Co_2Ni_2Ru yielded a lattice parameter of 3.58 Å, which closely matches the experimental value of 3.59 Å obtained from X-ray diffraction [25]. DPA produced the closest agreement with DFT (3.58 Å) with an error of −0.44%, while Orb and SevenNet overestimated a_0 by 0.58% and 2.32%, respectively. For pure Ni, all FPs showed good agreement with DFT (3.519 Å [73]), with Orb providing the most accurate prediction (0.14% error), followed by DPA and SevenNet with −0.36% and −0.45% deviations, respectively.

At 300 K, Orb did not preserve lattice stability in the examined materials and was consequently excluded from the analysis at this temperature. A direct comparison to DFT was unachievable due to the lack of reference DFT data. Nevertheless, both DPA

and SevenNet effectively replicate the anticipated thermal expansion characteristics of FCC alloys. For CoNiRu, the lattice parameter increased by 0.32% with DPA and 2.28% with SevenNet in comparison to their 0 K values. In Co_2Ni_2Ru, the expansions recorded were 0.11% (DPA) and 1.06% (SevenNet), whereas for pure Ni, the two FPs predicted increases of 0.29% and 0.37%, respectively.

Figure 2 shows the lattice parameters predicted by the SevenNet for FCC CoNiRu and FCC Co_2Ni_2Ru over system sizes ranging from ~2000 to ~30 000 atoms at 0 and 300 K. The values remain essentially size-independent, with variations of only ~0.10% and ~0.36% for CoNiRu and ~1.9% and ~1.8% for Co_2Ni_2Ru at 0 and 300 K, respectively. This confirms that SevenNet produces stable lattice parameter predictions that are insensitive to supercell size, at least for these two materials.

3.1.2 | HCP Materials

For the HCP systems, the basal length a_0 predicted by FPs at 0 K agrees closely with DFT. In CoNiRu, Orb provided the most accurate prediction, underestimating the DFT value (2.596 Å) by only 0.63%, followed by SevenNet (−1.00%) and DPA (−1.26%). In $CoNiRu_2$, where the DFT value is 2.645 Å, Orb achieved the smallest error (−1.16%), while DPA and SevenNet underestimated it by −1.48% and −1.40%, respectively. All three FPs therefore reproduce HCP a_0 within 1.5% of DFT.

For HCP CoNiRu, the DFT-calculated c lattice parameter was 4.126 Å. Among the FPs, DPA provided the most accurate prediction at 0 K with $c = 4.1167$ Å (−0.23% deviation), followed by SevenNet (4.1683 Å, +1.02%) and Orb (4.1929 Å, +1.62%). For HCP $CoNiRu_2$, the DFT result of 4.159 Å was also well reproduced, with DPA again showing the best agreement (4.1493 Å, −0.23%), while SevenNet (4.2264 Å, +1.62%) and Orb (4.2455 Å, +2.08%) slightly overestimated the value. At 300 K, no stable lattice configurations were obtained for Orb; hence, its results are not reported. DPA and SevenNet predicted $c = 4.1506$ Å (+0.82%) and 4.1147 Å (−1.29%), respectively, for CoNiRu, indicating minor thermal changes relative to 0 K. The negative thermal expansion predicted by SevenNet suggests limitations in its ability to accurately capture the temperature dependence of the lattice parameter, whereas DPA correctly predicted the positive thermal expansion. In contrast, $CoNiRu_2$ exhibited thermal expansion, with c increasing to 4.2118 Å (+1.51%) for DPA and 4.2411 Å (+0.35%) for SevenNet.

3.2 | Elastic Constants

First, we note that Orb exhibited poor results in predicting elastic constants for all materials at 0 K, on top of the fact that its elastic constants at 300 K are unobtainable due to the lattice instability at finite temperatures. For example, Orb significantly underestimates the mechanical stiffness of pure Ni, predicting a bulk modulus of only 2.36 GPa at 0 K—an unphysically low value compared with the DFT-calculated elastic constants ($C_{11}^* = 278.87$ GPa, $C_{12}^* = 158.83$ GPa, and $C_{44}^* = 132.18$ GPa) [73]. Consequently, this section focused exclusively on the results derived from the SevenNet and DPA models.

3.2.1 | FCC Materials

Figure 3 presents the calculated single-crystal effective elastic constants (C_{11}^*, C_{12}^*, and C_{44}^*) of FCC CoNiRu, Co_2Ni_2Ru, and pure Ni at 0 and 300 K. Results are compared against DFT at 0 K where available.

First, we focus on FCC CoNiRu. At 0 K, DFT reports $C_{11}^* = 404.43$ GPa, $C_{12}^* = 165.85$ GPa, and $C_{44}^* = 147.03$ GPa [27]. DPA systematically overestimates these values, predicting $C_{11}^* = 427.62$ GPa (+5.74%), $C_{12}^* = 237.25$ GPa (+43.06%), and $C_{44}^* = 178.56$ GPa (+21.49%) with a cell consisting of 20,328 atoms. SevenNet, on the other hand, underestimates C_{11}^* (321.23 GPa, −20.58%) and C_{44}^* (79.95 GPa, −45.61%), while overpredicting C_{12}^* (191.06 GPa, +15.17%) with a comparatively smaller cell of 6750 atoms. At 300 K, DFT data are unavailable. For CoNiRu, the SevenNet-based simulations were performed using a cell containing 11,664 atoms, whereas DPA used a significantly smaller cell with only 2,178 atoms at 300 K. SevenNet yields $C_{11}^* = 227.79$ GPa, $C_{12}^* = 228.53$ GPa, and $C_{44}^* = 114.52$ GPa, with strong softening in C_{44}^* (−42.9%) and C_{11}^* (−29.1%), but a significant increase in C_{12}^* (+19.6%). In the meantime, DPA shows a consistent reduction to $C_{11}^* = 320.29$ GPa, $C_{12}^* = 192.47$ GPa, and $C_{44}^* = 142.05$ GPa, corresponding to decreases of 25.1%, 18.9%, and 20.5%, respectively, relative to its 0 K values.

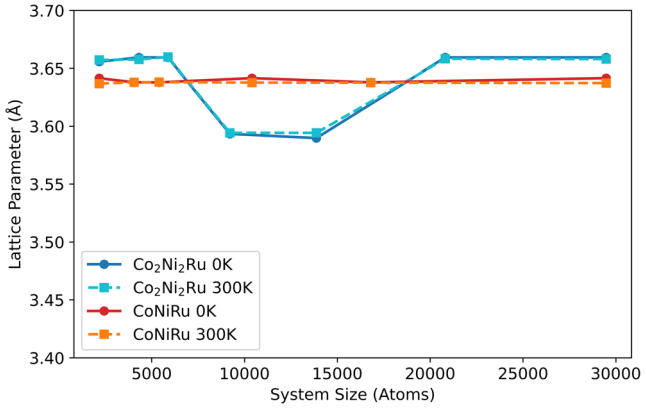

FIGURE 2 | SevenNet-based lattice parameters of FCC CoNiRu and Co_2Ni_2Ru at 0 and 300 K with varied supercell sizes.

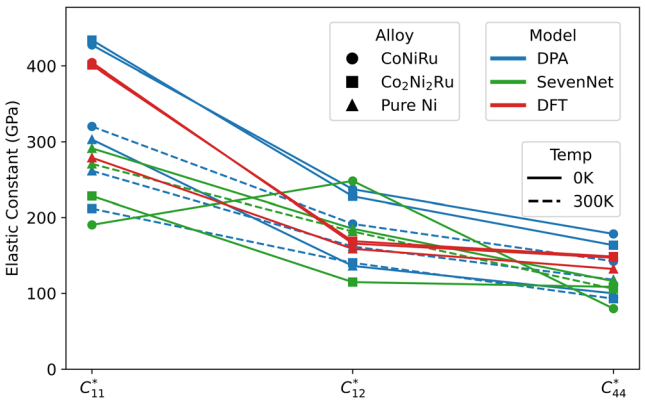

FIGURE 3 | Calculated elastic constants of FCC alloys and pure Ni at 0 and 300 K.

Next, we focus on FCC Co_2Ni_2Ru, for which no DFT reference is available, but large discrepancies between the two FPs are evident. The SevenNet-based simulations were performed using a consistent cell size of 11,664 atoms at both 0 K and 300 K. In contrast, DPA used a larger cell with 20 328 atoms at 0 K but a much smaller cell of 2,178 atoms at 300 K. SevenNet predicts $C_{11}^* = 303.41$ GPa, $C_{12}^* = 135.90$ GPa, and $C_{44}^* = 100.45$ GPa, whereas DPA predicts much higher values of $C_{11}^* = 434.23$ GPa, $C_{12}^* = 228.10$ GPa, and $C_{44}^* = 163.88$ GPa. At 300 K, SevenNet shows a weak-to-moderate temperature dependence, yielding $C_{11}^* = 292.11$ GPa (-3.7%), $C_{12}^* = 185.04$ GPa ($+36.1\%$), and $C_{44}^* = 115.73$ GPa ($+15.2\%$) compared to its 0 K predictions, while DPA exhibits pronounced softening, with $C_{11}^* = 212.45$ GPa, $C_{12}^* = 139.67$ GPa, and $C_{44}^* = 92.64$ GPa, corresponding to decreases of 51.1%, 38.8%, and 43.5%, respectively.

Last, we discuss results of FCC pure Ni. At 0 K, DFT provides $C_{11}^* = 278.87$ GPa, $C_{12}^* = 158.83$ GPa, and $C_{44}^* = 132.18$ GPa [73]. SevenNet employed a consistent cell size of 6,750 atoms at both 0 K and 300 K. In contrast, DPA simulations were conducted using a 20,328-atom cell at 0 K and a reduced 2,178-atom cell at 300 K. SevenNet yields $C_{11}^* = 291.65$ GPa ($+4.58\%$), $C_{12}^* = 185.13$ GPa ($+16.56\%$), and $C_{44}^* = 116.21$ GPa (-12.09%). In comparison, DPA slightly overestimates C_{11}^* (303.01 GPa, $+8.66\%$) but underestimates both C_{12}^* (136.22 GPa, -14.23%) and C_{44}^* (99.66 GPa, -24.58%), showing overall worse agreement with DFT than DPA. At 300 K, DFT data are not available, but SevenNet gives $C_{11}^* = 270.87$ GPa, $C_{12}^* = 181.93$ GPa, and $C_{44}^* = 106.27$ GPa, while DPA predicts $C_{11}^* = 261.77$ GPa, $C_{12}^* = 162.33$ GPa, and $C_{44}^* = 117.56$ GPa. Both FPs capture the expected thermal softening, with DPA showing strongerelative reductions in C_{11}^* (-13.6%) and C_{44}^* (-17.6%) than SevenNet.

3.2.2 | HCP Materials

Figure 4 shows the calculated single-crystal effective elastic constants (C_{11}^*, C_{12}^*, C_{13}^*, C_{33}^*, and C_{44}^*) for the HCP CoNiRu and $CoNiRu_2$ alloys at both 0 K and 300 K. Again, no elastic constant data exist for Orb because (i) its predictions are too low at 0 K and (ii) it results in unstable lattices at 300 K.

At 0 K, DFT predicted the elastic constants of HCP CoNiRu as $C_{11}^* = 377.03$ GPa, $C_{12}^* = 188.45$ GPa, $C_{13}^* = 137.2$ GPa, $C_{33}^* = 424.69$ GPa, and $C_{44}^* = 114.31$ GPa. Compared with these, DPA showed an overestimation in all components except C_{44}^*, with deviation percentages of +19.4% for C_{11}^*, +24.9% for C_{12}^*, +47.7% for C_{13}^*, +20.6% for C_{33}^*, and a moderate underestimation of -15.6% for C_{44}^* with discrepancies of -3.8% for C_{11}^*, +39.9% for C_{12}^*, +78.3% for C_{13}^*, +25.5% for C_{33}^*, and -25.2% for C_{44}^*. These trends highlight that while DPA captures the overall stiffness trends better, SevenNet suffers from inconsistent directional predictions.

At 300 K, DFT results were not available, so the thermal response was inferred by comparing each FP's predictions to their respective 0 K values. The DPA model exhibited modest reductions of less than 10% across all elastic constants (-0.1% for C_{11}^*, -9.8% for C_{12}^*, -8.9% for C_{13}^*, -9.7% for C_{33}^*, and -9.1% for C_{44}^*), indicating good thermal stability. In contrast, the SevenNet model showed pronounced softening, with decreases of -24.1%, -26.3%, -33.4%, -35.3%, and -32.6% for C_{11}^*, C_{12}^*, C_{13}^*, C_{33}^*, and C_{44}^*, respectively. These results suggest that DPA is more robust in capturing temperature-dependent behavior, whereas SevenNet tends to lose stiffness accuracy at elevated temperatures.

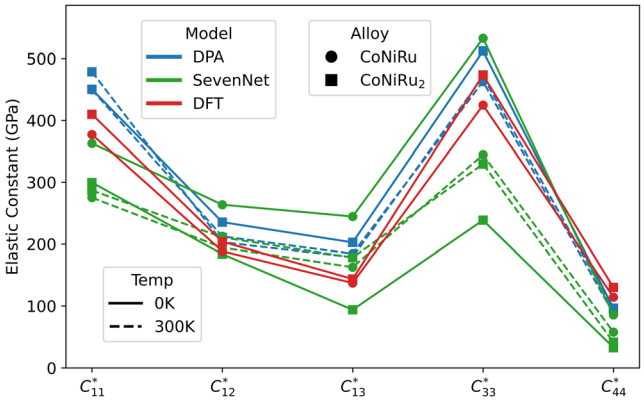

FIGURE 4 | Calculated elastic constants of HCP alloys at 0 and 300 K.

A similar comparison was carried out for the HCP $CoNiRu_2$ alloy. At 0 K, DFT calculations yielded $C_{11}^* = 409.68$ GPa, $C_{12}^* = 203.82$ GPa, $C_{13}^* = 143.67$ GPa, $C_{33}^* = 473.58$ GPa, and $C_{44}^* = 130.02$ GPa. DPA again overpredicted most values, with deviations of +9.9% for C_{11}^*, +15.5% for C_{12}^*, +41.0% for C_{13}^*, +8.2% for C_{33}^*, and an underestimation of -25.8% for C_{44}^*. In contrast, the SevenNet model exhibits larger discrepancies of -26.9%, -9.8%, -34.7%, -49.6%, and -74.8%, indicating significant underestimation, particularly in C_{33}^* and C_{44}^*. While both models maintain mechanical stability, DPA more accurately captures the DFT-predicted anisotropic elastic response of HCP $CoNiRu_2$. At 300 K, DFT data were unavailable; therefore, the thermal response was analyzed by comparing each potential's 300 K predictions to its 0 K values. The DPA model shows only minor variations, with changes of +6.3% for C_{11}^*, -13.8% for C_{12}^*, -11.7% for C_{13}^*, -0.3% for C_{33}^*, and -1.6% for C_{44}^*, indicating strong thermal stability and consistent elastic behavior across temperatures. In contrast, the SevenNet potential displays a less systematic trend, with deviations of -4.2%, +14.7%, +89.9%, +38.1%, and +26.2% for C_{11}^*, C_{12}^*, C_{13}^*, C_{33}^*, and C_{44}^*, respectively. The pronounced fluctuations, especially in C_{13}^* and C_{33}^*, suggest that SevenNet becomes less reliable under thermal perturbation, while DPA more accurately preserves the intrinsic stiffness characteristics of HCP $CoNiRu_2$ at elevated temperatures.

3.3 | USFE

Figure 5 illustrates the mean USFEs computed by the three FPs at 0 K. Particularly for the two FCC alloys, the distributions of USFE across different slip planes are shown in Figures 6 and 7. DFT values, when available, are displayed for comparison.

3.3.1 | FCC Materials

For FCC CoNiRu, the DFT value for mean USFE is 376.41 mJ/m^2 [27]. DPA projects a somewhat higher USFE of 394.32 mJ/m^2, which amounts to a 4.8% overestimation. While SevenNet provides the lowest prediction of 200.35 mJ/m^2, underestimating

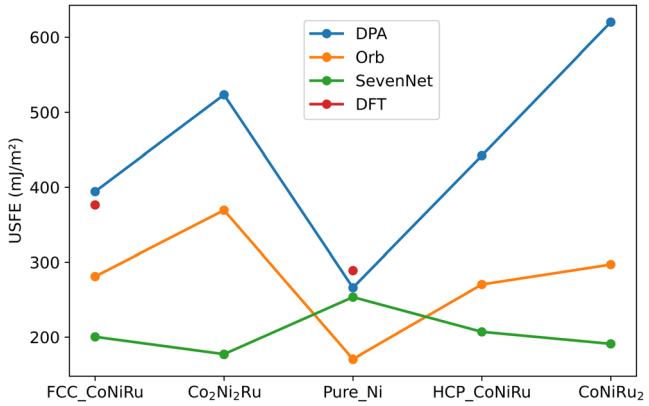

FIGURE 5 | Calculated mean USFE of FCC alloys, HCP alloys, and pure Ni at 0 K.

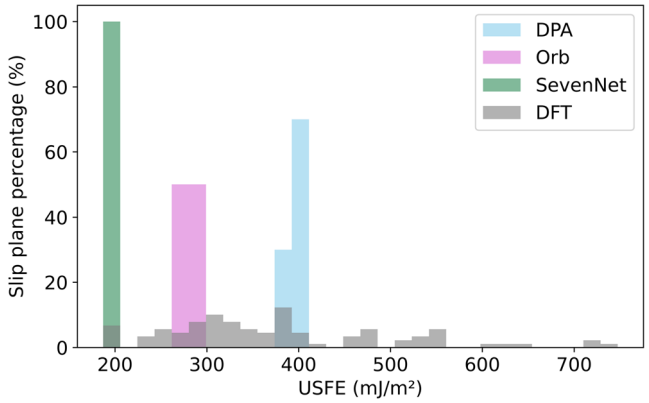

FIGURE 6 | Distribution of USFE values of FCC CoNiRu. Those based on DFT were previously published as Su et al. [27].

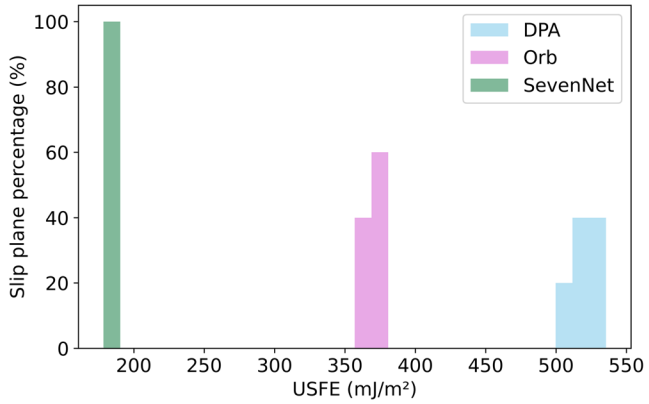

FIGURE 7 | Distribution of USFE values of FCC Co_2Ni_2Ru.

by 46.8%, Orb underestimates the USFE at 280.99 mJ/m^2, which corresponds to a −25.4% deviation from DFT. The histogram in Figure 6 highlights these trends: DPA's distribution is centered near the DFT reference with a narrow spread, whereas Orb and SevenNet shift significantly toward lower energies.

For FCC Co_2Ni_2Ru, there is no DFT benchmark available. However, a significant divergence among FPs is observed. DPA produces the highest mean USFE at 523.48 mJ/m^2, followed by Orb at 369.40 mJ/m^2 and SevenNet at 177.17 mJ/m^2. The histograms in Figure 7 clearly show the distinct clustering of predictions, with DPA capturing the upper limit and SevenNet indicating considerably lower USFE. The challenge of consistent GSFE prediction in chemically complex systems and the necessity of reference-level validation are underscored by the variation among the three FPs, which exceeds 340 mJ/m^2.

For pure Ni, the DFT-calculated USFE at 0 K is 289 mJ/m^2 [73]. Among the FPs, DPA predicts a value of 266.05 mJ/m^2, which underestimates the DFT reference by approximately 8.0%. The Orb model yields a slightly lower value of 170.63 mJ/m^2, corresponding to a larger deviation of about 40.9%. In contrast, SevenNet produces 253.49 mJ/m^2, underestimating the DFT result by 12.3%. Overall, DPA exhibits the closest agreement with DFT, while Orb significantly underpredicts the USFE.

3.3.2 | HCP Materials

For HCP CoNiRu, DFT data is also unavailable. DPA predicts the USFE at 442.22 mJ/m^2, Orb indicates 270.42 mJ/m^2, and SevenNet presents the lowest value at 207.04 mJ/m^2. This trend agrees with that in FCC materials, where DPA typically forecasts higher USFEs while SevenNet exhibits lower values. The disparity between DPA and SevenNet in this system exceeds 235 mJ/m^2, signifying substantial model reliance in forecasting basal-plane fault energy in HCP structures.

For HCP $CoNiRu_2$, for which DFT reference data is also unavailable, a comparable trend is noted. DPA achieves the greatest USFE of 620.24 mJ/m^2, followed by Orb at 297.01 mJ/m^2 and SevenNet at 190.97 mJ/m^2. All results consistently point to that DPA forecasts elevated USFEs while SevenNet predicts reduced ones.

3.4 | ISFE

Figure 8 displays the mean ISFE values computed by the three FPs at 0 K. Particularly for each of the two FCC alloys, the distributions of ISFE among different slip planes are shown in Figures 9 and 10. DFT values are utilized as benchmarks, if applicable, to evaluate the accuracy of the FP predictions.

3.4.1 | FCC Materials

For FCC CoNiRu, DFT predicts that the mean ISFE is −44.56 mJ/m^2, while the ISFE values range from approximately −300 to +150 mJ/m^2 [27]. Among the FPs, DPA offers a partial reproduction of the negative ISFE tail, although it underestimates the extremes; the mean ISFE value is −39.77 mJ/m^2, exhibiting a variance of 10.7% with respect to DFT. Conversely, Orb (2.36 mJ/m^2) and SevenNet (5.92 mJ/m^2) yield erroneous positive mean ISFE value, failing to replicate the fault instability identified by DFT. In terms of the distribution, Orb and SevenNet yield narrow, unimodal peaks near 0–20 mJ/m^2, missing the broad, asymmetric spread in DFT; in other words, these two models fail to capture faulting diversity, limiting their fidelity in modeling defect energetics.

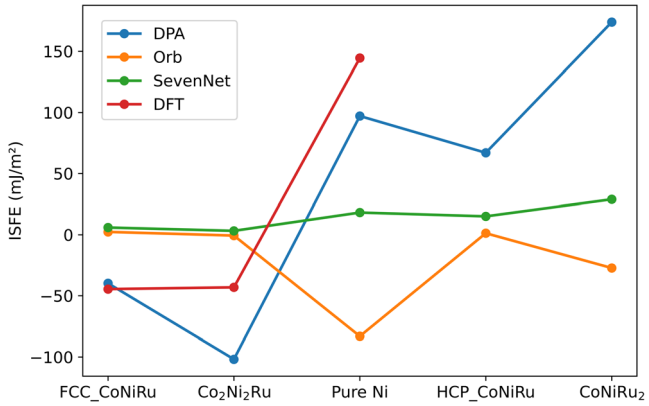

FIGURE 8 | Calculated mean ISFE of FCC alloys, HCP alloys, and pure Ni at 0 K.

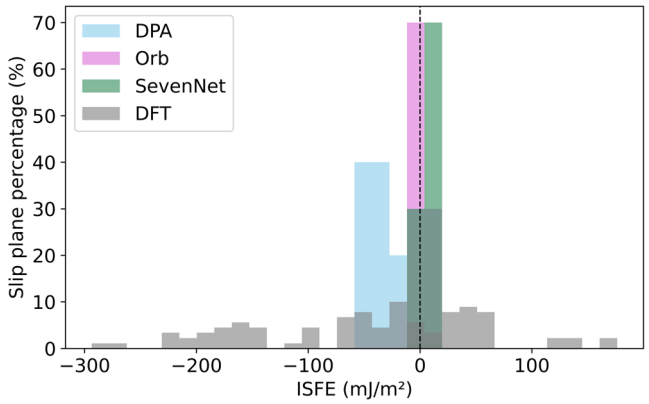

FIGURE 9 | Distribution of ISFE values of FCC CoNiRu. Those based on DFT were previously published as Su et al. [27].

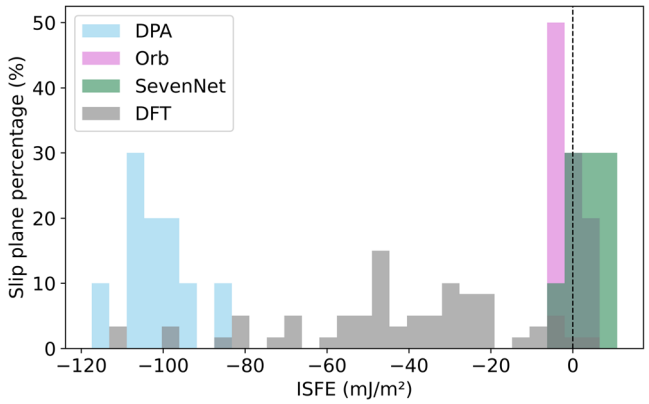

FIGURE 10 | Distribution of ISFE values of FCC Co_2Ni_2Ru.

For FCC Co_2Ni_2Ru, the DFT calculation of ISFE was computed from 60 different slip planes, with the mean value being −43.11 mJ/m^2. The distribution predominantly spans from −120 to a few mJ/m^2. Among the three FPs, DPA provides the best qualitative overlap, particularly in reproducing some negative ISFE values. However, its mean ISFE value is −101.89 mJ/m^2, resulting in a deviation of approximately 136.2% with respect to DFT. On the other hand, Orb and SevenNet remain confined to narrow distributions centered near zero, significantly diverging from the DFT-predicted spread. In terms of the mean ISFE value, SevenNet offers a closer-than-DPA approximation at 3.21 mJ/m^2, though it still deviates by 107.4% from the DFT reference. The Orb model predicts a similar mean ISFE value of −0.65 mJ/m^2, corresponding to a deviation of 98.5%.

For FCC pure Ni, the DFT prediction is 144.50 mJ/m^2. DPA approximates this at 97.14 mJ/m^2, resulting in a discrepancy of −32.8%. SevenNet exhibits a significantly greater deviation with a prediction of 18.20 mJ/m^2, whereas Orb forecasts an erroneous negative value of −83.15 mJ/m^2, diverging from DFT by more than −150%.

These results emphasize the challenges that current FPs face in capturing the complex fault energy landscape of MPEAs, with none of the models well matching DFT.

3.4.2 | HCP Materials

For HCP CoNiRu, where DFT data are unavailable, DPA predicts an ISFE of 66.98 mJ/m^2, followed by SevenNet at 15.07 mJ/m^2 and Orb at 1.27 mJ/m^2.

For HCP $CoNiRu_2$, for which DFT data also do not exist, DPA predicts the highest ISFE at 173.90 mJ/m^2, while SevenNet and Orb yield significantly lower values of 28.90 mJ/m^2 and −27.25 mJ/m^2, respectively, with Orb again misrepresenting the sign.

4 | Conclusion

This study systematically assessed three FPs—SevenNet, DPA, and Orb—for predicting selected properties of Co–Ni–Ru-based MPEAs and pure Ni. The properties investigated encompass lattice parameters, elastic constants, USFEs, and ISFEs, with comparisons to DFT values wherever available.

All FPs exhibited reasonably precise predictions of lattice parameters, with errors typically under 2.5% at 0 K. Orb demonstrated superior performance for HCP structures at 0 K, but DPA consistently correlated better with DFT for FCC alloys at 0 K. Both DPA and SevenNet captured the expected thermal expansion behavior, exhibiting increased lattice parameters at 300 K relative to 0 K, while Orb was excluded from the simulations due to its lattice instability at 300 K.

For FCC structured systems, the elastic constants at 0 K show clear deviations between DPA, SevenNet, and DFT benchmarks. For FCC CoNiRu, DPA overestimated all three constants (C_{11}^*, C_{12}^*, C_{44}^*), with particularly large errors in C_{12}^*, while SevenNet severely underestimated C_{11}^* and C_{44}^* and moderately overpredicted C_{12}^*. At 300 K, both models reflected expected softening trends, although SevenNet showed more pronounced drops in C_{11}^* and C_{44}^*, and an unusual increase in C_{12}^*. DPA, by contrast, maintained more consistent reductions across all constants. In FCC Co_2Ni_2Ru, where no DFT data are available, DPA predicted significantly stiffer elastic behavior than SevenNet at 0 K. As temperature increased, SevenNet exhibited moderate variation with some stiffening in C_{12}^* and C_{44}^*, while DPA underwent dramatic

softening—dropping over 40% in all components. For pure Ni, both models captured general elastic trends reasonably well, but DPA underestimated C_{12}^* and C_{44}^*, while SevenNet produced closer agreement with DFT, particularly for C_{11}^* and C_{12}^*. At elevated temperature, both FPs predicted thermal softening, with DPA showing stronger reductions in C_{11}^* and C_{44}^* than SevenNet. Overall, DPA tends to overpredict stiffness at low temperatures but shows stronger temperature dependence, while SevenNet offers better agreement for some components but suffers from inconsistent trends under thermal perturbation.

For HCP structured systems, DPA generally overestimated the elastic constants of CoNiRu at 0 K, with a large deviation in C_{13}^* and moderate underestimation of C_{44}^* from DFT results. SevenNet, in contrast, severely underestimated C_{11}^* and C_{44}^* while overpredicting C_{12}^* and C_{13}^*, indicating inconsistent performance. At 300 K, DPA showed stable thermal behavior with less than 10% reduction across constants, while SevenNet exhibited substantial softening, particularly in C_{13}^*, C_{33}^*, and C_{44}^*. For $CoNiRu_2$, DPA again overestimated most constants at 0 K and showed good temperature stability at 300 K, especially for C_{44}^*, which changed by only −1.6%. SevenNet data were unavailable for this case. Overall, DPA provided more consistent and reliable predictions across both alloys and temperatures, whereas SevenNet showed greater variability and limited applicability.

Significant variation in USFE predictions is observed across the FPs. For FCC CoNiRu and pure Ni, DPA shows the closest agreement with DFT, while SevenNet tends to significantly underpredict and Orb falls somewhere in between. This pattern holds across both FCC and HCP structures, where DPA consistently forecasts higher fault energies, SevenNet predicts lower values, and Orb shows variable performance. The discrepancies become even more pronounced in chemically complex alloys like Co_2Ni_2Ru, where model predictions diverge widely. For HCP CoNiRu and $CoNiRu_2$, where DFT data is unavailable, DPA consistently predicts the highest USFEs, SevenNet the lowest, and Orb lies in between.

ISFE predictions across FCC and HCP systems reveal further inconsistencies among FPs. For FCC CoNiRu, DPA closely aligns with the DFT reference, while Orb and SevenNet fail to capture the fault instability, incorrectly predicting positive values. In FCC Co_2Ni_2Ru, all models deviate significantly from the DFT-based mean, with DPA overestimating and both Orb and SevenNet underperforming, highlighting the difficulty of modeling stacking faults in chemically complex alloys. For pure Ni, DPA moderately underestimates the ISFE, SevenNet underpredicts severely, and Orb incorrectly outputs a negative value. In HCP systems, where DFT data are unavailable, the same trend persists: DPA consistently predicts the highest ISFEs, while SevenNet and Orb yield much lower values, with Orb again misrepresenting the sign in $CoNiRu_2$. These results underscore the model-dependent nature of ISFE predictions and the challenge of achieving accurate fault energy estimation in MPEAs.

For GSFE overall, DPA exhibited the most accurate correlation with DFT in both USFE and ISFE estimations. Conversely, Orb and SevenNet frequently misrepresented the sign or amplitude of ISFE, particularly in HCP systems.

Taken together, our findings emphasize that although FPs offer substantial promise for modeling MPEAs, their quantitative reliability varies significantly across property classes and potential types. This study provides a baseline for evaluating FPs in MPEAs, underscoring the need for systematic validation before deployment in predictive simulations of plasticity and defect behavior. Our work highlights that the selection of FPs might result in substantial disparities, even in the prediction of basic material properties such as elastic constants. Future work could include finite-temperature DFT benchmarks for HCP systems and investigation of additional defect energetics such as vacancies and twin boundaries. Dynamic simulations involving dislocations or deformation can further assess the transferability of FPs under realistic conditions.

Acknowledgments

S.M. and S.X. acknowledge the ORAU Ralph E. Powe Junior Faculty Enhancement Award. Some of the computing for this project was performed at the OU Supercomputing Center for Education & Research at the University of Oklahoma (OU). S.S. and B.W. appreciate support from the U.S. Department of Energy, Office of Science, Basic Energy Sciences under award number DE-SC0018284. Their computational simulations used supercomputer resources of the National Energy Research Scientific Computing Center, a U.S. Department of Energy Office of Science User Facility. Partial calculations were performed by M.H. at Theia, an AI-focused HPC cluster at the University of South Carolina supported by the U.S. National Science Foundation (award number 2320292). I.G. acknowledges support from the Samuel Roberts Noble Microscopy Laboratory at OU. Financial support was provided by the OU Libraries' Open Access Fund. [Correction added on 15 June 2026, after first online publication: The acknowledgement section has been corrected.]

Funding

This work was supported by the ORAU Ralph E. Powe Junior Faculty Enhancement Award, U.S. Department of Energy, Office of Science, Basic Energy Sciences (DE-SC0018284), U.S. National Science Foundation (2320292), National Energy Research Scientific Computing Center (NERSC), Samuel Roberts Noble Microscopy Laboratory at OU.

Conflicts of Interest

The authors declare no conflicts of interest.

Data Availability Statement

The data that support the findings of this study are openly available in this GitHub repository: https://github.com/shuozhixu/AID_2026.

References

1. O. N. Senkov, D. B. Miracle, K. J. Chaput, and J.-P. Couzinie, "Development and Exploration of Refractory High Entropy Alloys—A Review," *Journal of Materials Research* 33, no. 19 (October 2018): 3092.

2. J.-W. Yeh, S.-K. Chen, S.-J. Lin, et al., "Nanostructured High-Entropy Alloys with Multiple Principal Elements: Novel Alloy Design Concepts and Outcomes," *Advanced Engineering Materials* 6, no. 5 (2004): 299.

3. D. B. Miracle and O. N. Senkov, "A Critical Review of High Entropy Alloys and Related Concepts," *Acta Materialia* 122 (January 2017): 448.

4. Y. Zhang, T. T. Zuo, Z. Tang, et al., "Microstructures and Properties of High-Entropy Alloys," Progress in Materials Science 61 (April 2014): 1.

5. Z. Li, K. G. Pradeep, Y. Deng, D. Raabe, and C. C. Tasan, "Metastable High-Entropy Dual-Phase Alloys Overcome the Strength–ductility Trade-Off," *Nature* 534, no. 7606 (June 2016): 227.

6. Y. Yao, Z. Huang, P. Xie, et al., "Carbothermal Shock Synthesis of High-Entropy-Alloy Nanoparticles," *Science* 359, no. 6383 (March 2018): 1489.

7. P. Xie, Y. Yao, Z. Huang, et al., "Highly Efficient Decomposition of Ammonia Using High-Entropy Alloy Catalysts," *Nature Communications* 10, no. 1 (September 2019): 4011.

8. S. I. Rao, C. Woodward, T. A. Parthasarathy, and O. Senkov, "Atomistic Simulations of Dislocation Behavior in a Model FCC Multicomponent Concentrated Solid Solution Alloy," *Acta Materialia* 134 (August 2017): 188.

9. S. I. Rao, B. Akdim, E. Antillon, C. Woodward, T. A. Parthasarathy, and O. N. Senkov, "Modeling Solution Hardening in BCC Refractory Complex Concentrated Alloys: NbTiZr, Nb1.5TiZr0.5 and Nb0.5TiZr1.5," *Acta Materialia* 168 (April 2019): 222.

10. F. Maresca and W. A. Curtin, "Mechanistic Origin of High Strength in Refractory BCC High Entropy Alloys up to 1900K," *Acta Materialia* 182 (January 2020): 235.

11. A. Gali and E. P. George, "Tensile Properties of High- and Medium-Entropy Alloys," *Intermetallics* 39 (August 2013): 74.

12. F. Otto, A. Dlouhý, C. Somsen, H. Bei, G. Eggeler, and E. P. George, "The Influences of Temperature and Microstructure on the Tensile Properties of a CoCrFeMnNi High-Entropy Alloy," *Acta Materialia* 61, no. 15 (September 2013): 5743.

13. M. N. Hasan, Y. F. Liu, X. H. An, et al., "Simultaneously Enhancing Strength and Ductility of a High-Entropy Alloy via Gradient Hierarchical Microstructures," *International Journal of Plasticity* 123 (December 2019): 178.

14. K. Ming, X. Bi, and J. Wang, "Strength and Ductility of CrFeCoNiMo Alloy with Hierarchical Microstructures," *International Journal of Plasticity* 113 (February 2019): 255.

15. M. Schneider, E. P. George, T. J. Manescau, et al., "Analysis of Strengthening due to Grain Boundaries and Annealing Twin Boundaries in the CrCoNi Medium-Entropy Alloy," *International Journal of Plasticity* 124 (January 2020): 155.

16. J. Brechtl, S. Y. Chen, X. Xie, et al., "Towards a Greater Understanding of Serrated Flows in an Al-Containing High-Entropy-Based Alloy," *International Journal of Plasticity* 115 (April 2019): 71.

17. Z. Li, S. Zhao, R. O. Ritchie, and M. A. Meyers, "Mechanical Properties of High-Entropy Alloys with Emphasis on Face-Centered Cubic Alloys," Progress in Materials Science 102 (May 2019): 296.

18. Z. Wu, H. Bei, G. M. Pharr, and E. P. George, "Temperature Dependence of the Mechanical Properties of Equiatomic Solid Solution Alloys with Face-Centered Cubic Crystal Structures," *Acta Materialia* 81 (2014): 428.

19. B. Gludovatz, A. Hohenwarter, K. V. S. Thurston, et al., "Exceptional Damage-Tolerance of a Medium-Entropy Alloy CrCoNi at Cryogenic Temperatures," *Nature Communications* 7, no. 1 (February 2016): 10602.

20. S. F. Liu, Y. Wu, H. T. Wang, et al., "Stacking Fault Energy of Face-Centered-Cubic High Entropy Alloys," *Intermetallics* 93 (February 2018): 269.

21. G. Laplanche, A. Kostka, C. Reinhart, J. Hunfeld, G. Eggeler, and E. P. George, "Reasons for the Superior Mechanical Properties of Medium-Entropy CrCoNi Compared to High-Entropy CrMnFeCoNi," *Acta Materialia* 128 (April 2017): 292.

22. G. Laplanche, A. Kostka, O. M. Horst, G. Eggeler, and E. P. George, "Microstructure Evolution and Critical Stress for Twinning in the CrMnFeCoNi High-Entropy Alloy," *Acta Materialia* 118 (October 2016): 152.

23. J. Miao, C. E. Slone, T. M. Smith, et al., "The Evolution of the Deformation Substructure in a Ni-Co-Cr Equiatomic Solid Solution Alloy," *Acta Materialia* 132 (June 2017): 35.

24. E. P. George, D. Raabe, and R. O. Ritchie, "High-Entropy Alloys," *Nature Reviews Materials* 4, no. 8 (August 2019): 515.

25. M. A. Charpagne, K. V. Vamsi, Y. M. Eggeler, et al., "Design of Nickel-Cobalt-Ruthenium Multi-Principal Element Alloys," *Acta Materialia* 194 (August 2020): 224.

26. H. Warlimont and W. Martienssen, eds., *Springer Handbook of Materials Data*, 2nd ed. (Springer International Publishing, 2018).

27. Y. Su, S. Xu, and I. J. Beyerlein, "Ab Initio -Informed Phase-Field Modeling of Dislocation Core Structures in Equal-Molar CoNiRu Multi-Principal Element Alloys," Modelling and Simulation in Materials Science and Engineering 27, no. 8 (August 2019): 084001.

28. J. Behler, "Perspective: Machine Learning Potentials for Atomistic Simulations," *Journal of Chemical Physics* 145, no. 17 (November 2016): 170901.

29. J. Graser, S. K. Kauwe, and T. D. Sparks, "Machine Learning and Energy Minimization Approaches for Crystal Structure Predictions: A Review and New Horizons," *Chemistry of Materials* 30, no. 11 (June 2018): 3601.

30. J. Schmidt, M. R. G. Marques, S. Botti, and M. A. L. Marques, "Recent Advances and Applications of Machine Learning in Solid-State Materials Science," *npj Computational Materials* 5, no. 1 (August 2019): 83.

31. O. T. Unke, S. Chmiela, H. E. Sauceda, et al., "Machine Learning Force Fields," *Chemical Reviews* 121, no. 16 (August 2021): 10142.

32. E. Berger, M. Bagheri, and H.-P. Komsa, "CO_2 and Temperature Induced Switching of a Flexible Metal–Organic Framework with Surface-Mounted Nanoparticles," *Small* 21, no. 37 (2025): e03956.

33. T. B. Blank, S. D. Brown, A. W. Calhoun, and D. J. Doren, "Neural Network Models of Potential Energy Surfaces," *Journal of Chemical Physics* 103, no. 10 (September 1995): 4129.

34. A. P. Bartók, M. C. Payne, R. Kondor, and G. Csányi, "Gaussian Approximation Potentials: The Accuracy of Quantum Mechanics, without the Electrons," *Physical Review Letters* 104, no. 13 (April 2010): 136403.

35. C. Chen, W. Ye, Y. Zuo, C. Zheng, and S. P. Ong, "Graph Networks as a Universal Machine Learning Framework for Molecules and Crystals," *Chemistry of Materials* 31, no. 9 (May 2019): 3564.

36. K. Song, S. Käser, K. Töpfer, L. I. Vazquez-Salazar, and M. Meuwly, "PhysNet Meets CHARMM: A Framework for Routine Machine Learning/Molecular Mechanics Simulations," *Journal of Chemical Physics* 159, no. 2 (July 2023): 024125.

37. A. Jain, S. P. Ong, G. Hautier, et al., "Commentary: The Materials Project: A Materials Genome Approach to Accelerating Materials Innovation," *APL Materials* 1, no. 1 (July 2013): 011002.

38. S. Kirklin, J. E. Saal, B. Meredig, et al., "The Open Quantum Materials Database (OQMD): Assessing the Accuracy of DFT Formation Energies," *npj Computational Materials* 1, no. 1 (December 2015): 15010.

39. S. Curtarolo, W. Setyawan, S. Wang, et al., "AFLOWLIB.ORG: A Distributed Materials Properties Repository from High-Throughput Ab Initio Calculations," *Computational Materials Science* 58 (June 2012): 227.

40. J. Schmidt, T. F. T. Cerqueira, A. H. Romero, et al., "Improving Machine-Learning Models in Materials Science through Large Datasets," *Materials Today Physics* 48 (November 2024): 101560.

41. M. Scheidgen, L. Himanen, A. N. Ladines, et al., "NOMAD: A Distributed Web-Based Platform for Managing Materials Science Research Data," *Journal of Open Source Software* 8, no. 90 (October 2023): 5388.

42. C. Chen and S. P. Ong, "A Universal Graph Deep Learning Interatomic Potential for the Periodic Table," *Nature Computational Science* 2 (2022): 718.

43. A. Hajibabaei and K. S. Kim, "Universal Machine Learning Interatomic Potentials: Surveying Solid Electrolytes," *Journal of Physical Chemistry Letters* 12, no. 33 (2021): 8115.

44. A. Loew, D. Sun, H.-C. Wang, S. Botti, and M. A. L. Marques, "Universal Machine Learning Interatomic Potentials Are Ready for Phonons," *npj Computational Materials* 11, no. 1 (June 2025): 178.

45. X. Huang, B. Deng, P. Zhong, A. D. Kaplan, K. A. Persson, and G. Ceder, "Cross-Functional Transferability in Foundation Machine Learning Interatomic Potentials," *npj Computational Materials* 11, no. 1 (October 2025): 313.

46. K. S. Jakob, K. Reuter, and J. T. Margraf, "Universally Accurate or Specifically Inadequate? Stress-Testing General Purpose Machine Learning Interatomic Potentials," *Advanced Intelligent Discovery* 1 (2025): 202500031.

47. H. Yu, M. Giantomassi, G. Materzanini, J. Wang, and G.-M. Rignanese, "Systematic Assessment of Various Universal Machine-Learning Interatomic Potentials," *Materials Genome Engineering Advances* 2, no. 3 (2024): e58.

48. B. Focassio, L. P. M. Freitas, and G. R. Schleder, "Performance Assessment of Universal Machine Learning Interatomic Potentials: Challenges and Directions for Materials' Surfaces," *ACS Applied Materials & Interfaces* 17, no. 9 (March 2025): 13111.

49. L. Casillas-Trujillo, A. S. Parackal, R. Armiento, and B. Alling, "Evaluating and Improving the Predictive Accuracy of Mixing Enthalpies and Volumes in Disordered Alloys from Universal Pretrained Machine Learning Potentials," *Physical Review Materials* 8, no. 11 (November 2024): 113803.

50. B. Deng, Y. Choi, P. Zhong, et al., "Systematic Softening in Universal Machine Learning Interatomic Potentials," *npj Computational Materials* 11, no. 1 (January 2025): 9.

51. D. Zhang, X. Liu, X. Zhang, et al., "DPA-2: A Large Atomic Model as a Multi-Task Learner," *npj Computational Materials* 10, no. 1 (December 2024): 293.

52. Y. Park, J. Kim, S. Hwang, and S. Han, "Scalable Parallel Algorithm for Graph Neural Network Interatomic Potentials in Molecular Dynamics Simulations," *Journal of Chemical Theory and Computation* 20, no. 11 (June 2024): 4857.

53. M. Neumann, J. Gin, B. Rhodes, et al., "Orb: A Fast, Scalable Neural Network Potential," October 31, 2024, http://arxiv.org/abs/2410.22570.

54. S. Batzner, A. Musaelian, L. Sun, et al., "E (3)-Equivariant Graph Neural Networks for Data-Efficient and Accurate Interatomic Potentials," *Nature Communications* 13, no. 1 (May 2022): 2453.

55. A. Sanchez-Gonzalez, J. Godwin, T. Pfaff, R. Ying, J. Leskovec, and P. W. Battaglia, "Learning to Simulate Complex Physics with Graph Networks," ICML'20: Proceedings of the 37th International Conference on Machine Learning, (2020): 8459–8468.

56. A. P. Bartók, R. Kondor, and G. Csányi, "On Representing Chemical Environments," *Physical Review B* 87, no. 18 (May 2013): 184115.

57. Y. Liu, H. Zhang, Y. Yang, et al., "Chemical Short-range Order Dependence of Micromechanical Behavior in CoCrNi Medium-entropy Alloy Studied by Atomic Simulations," *Journal of Alloys and Compounds*968, (December 2023): 172002.

58. X. Yang, Y. Xi, C. He, H. Chen, X. Zhang, and S. Tu, "Chemical Short-range Order Strengthening Mechanism in CoCrNi Medium-entropy Alloy Under Nanoindentation," *Scripta Materialia* 209, (2022): 114364.

59. S. Mubassira, W.-R. Jian, and S. Xu, "Effects of Chemical Short-Range Order and Temperature on Basic Structure Parameters and Stacking Fault Energies in Multi-Principal Element Alloys," *Modelling* 5, no. 1 (March 2024): 352.

60. S. Yin, Y. Zuo, A. Abu-Odeh, et al., "Atomistic Simulations of Dislocation Mobility in Refractory High-entropy Alloys and the Effect of Chemical Short-range Order," *Nature Communications* 12, no. 1 (2021): 4873. Nature Publishing Group.

61. H. Zheng, L. T. W. Fey, X.-G. Li, et al., "Multi-scale Investigation of Short-range Order and Dislocation Glide in MoNbTi and TaNbTi Multi-principal Element Alloys," *npj Computational Materials* 9, no. 1 (2023): 89.

62. W.-R. Jian, S. Xu, D. Chen, and I. J. Beyerlein, "Chemical Short-range Order Enhances Fracture Toughness of Medium Entropy Alloy CoCrNi," *Applied Physics Letters* 124 (2024): 171903.

63. B. Wu, Y. Zhao, H. Ali, et al., "A Reasonable Approach to Describe the Atom Distributions and Configurational Entropy in High Entropy Alloys Based on Site Preference," *Intermetallics* 144 (2022): 107489.

64. L. Weng, X. Zhang, L. Su, et al., "Prediction of the Catalytic Mechanism of Hydrogen Evolution Reaction Enhanced by Surface Oxidation on FCC_CoCrFeNi and Co0.35Cr0.15Fe0.2Mo0.1Ni0.2 Multi-Principal Element Alloys Based on Site Preference," *Applied Surface Science* 672 (2024): 160730.

65. L. Su, H. Que, C. Qian, et al., "Prediction of Oxygen Evolution Reaction Activity of FCC_CoCuFeNiPd and CoCuFeNiRu Multi-Principal Element Alloys Based on Sublattice Preference of Constituent Atoms and the Site Preference of Intermediates," *Physical Chemistry Chemical Physics* 27, no. 41 (2025): 22064.

66. C. Zhang, C. Qian, Z. Ye, et al., "Influence of Ordering Behaviors on Thermodynamic and Mechanical Properties of FCC_CoNiV Multi-Principal Element Alloys," Transactions of Nonferrous Metals Society of China 35, no. 7 (2025): 2320.

67. R. Chen, L. Weng, C. Zhang, et al., "The Influence of Site Preference on the Elastic Properties of FCC_CoCrFeNi Multi-Principal Element Alloy," *Journal of Alloys and Compounds* 965 (2023): 171426.

68. A. P. Thompson, H. M. Aktulga, R. Berger, et al., "LAMMPS-A Flexible Simulation Tool for Particle-Based Materials Modeling at the Atomic, Meso, and Continuum Scales," *Computer Physics Communications* 271 (February 2022): 108171.

69. P. Hirel, "Atomsk: A Tool for Manipulating and Converting Atomic Data Files," *Computer Physics Communications* 197 (December 2015): 212.

70. MDIL-SNU, Sevennet: Pretrained Potentials Repository, 2024, https://github.com/MDIL-SNU/SevenNet/tree/main/sevenn/pretrained_potentials/SevenNet_022May2024.

71. J. Gilmer, S. S. Schoenholz, P. F. Riley, O. Vinyals, and G. E. Dahl, "Neural Message Passing for Quantum Chemistry," in ICML'17: Proceedings of the 34th International Confernce on Machine Learning 70 (2017): 1263–1272.

72. J. Zeng, D. Zhang, A. Peng, et al., "DeePMD-kit v3: A Multiple-Backend Framework for Machine Learning Potentials," *Journal of Chemical Theory and Computation* 21, no. 9 (May 2025): 4375.

73. Y. Su, S. Xu, and I. J. Beyerlein, "Density Functional Theory Calculations of Generalized Stacking Fault Energy Surfaces for Eight Face-Centered Cubic Transition Metals," *Journal of Applied Physics* 126, no. 10 (September 2019): 105112.

74. G. Kresse and J. Hafner, "Ab Initio Molecular Dynamics for Liquid Metals," *Physical Review B* 47, no. 1 (January 1993): 558.

75. G. Kresse and J. Furthmüller, "Efficiency of Ab-Initio Total Energy Calculations for Metals and Semiconductors Using a Plane-Wave Basis Set," *Computational Materials Science* 6, no. 1 (July 1996): 15.

76. M. Methfessel and A. T. Paxton, "High-Precision Sampling for Brillouin-Zone Integration in Metals," *Physical Review B* 40, no. 6 (August 1989): 3616.

77. H. J. Monkhorst and J. D. Pack, "Special Points for Brillouin-Zone Integrations," *Physical Review B* 13, no. 12 (June 1976): 5188.

78. J. P. Perdew, K. Burke, and M. Ernzerhof, "Generalized Gradient Approximation Made Simple," *Physical Review Letters* 77, no. 18 (October 1996): 3865.

79. P. E. Blöchl, "Projector Augmented-Wave Method," *Physical Review B* 50, no. 24 (December 1994): 17953.

80. G. Kresse and D. Joubert, "From Ultrasoft Pseudopotentials to the Projector Augmented-Wave Method," *Physical Review B* 59, no. 3 (January 1999): 1758.

81. X. Wang, S. Xu, W.-R. Jian, X.-G. Li, Y. Su, and I. J. Beyerlein, "Generalized Stacking Fault Energies and Peierls Stresses in Refractory Body-Centered Cubic Metals from Machine Learning-Based Interatomic Potentials," *Computational Materials Science* 192 (May 2021): 110364.

82. S. Xu, E. Hwang, W.-R. Jian, Y. Su, and I. J. Beyerlein, "Atomistic Calculations of the Generalized Stacking Fault Energies in Two Refractory Multi-Principal Element Alloys," *Intermetallics* 124 (September 2020): 106844.

83. J. R. Ray and A. Rahman, "Statistical Ensembles and Molecular Dynamics Studies of Anisotropic Solids," *Journal of Chemical Physics* 80, no. 9 (May 1984): 4423.

84. A. R. Natarajan and A. Van der Ven, "Linking Electronic Structure Calculations to Generalized Stacking Fault Energies in Multicomponent Alloys," *npj Computational Materials* 6, no. 1 (June 2020): 80.

85. Z. Pei, L.-F. Zhu, M. Friák, et al., "Ab Initio and Atomistic Study of Generalized Stacking Fault Energies in Mg and Mg–Y Alloys," *New Journal of Physics* 15, no. 4 (April 2013): 043020.

86. J. Ding, Q. Yu, M. Asta, and R. O. Ritchie, "Abiotic Synthesis of Purine and Pyrimidine Ribonucleosides in Aqueous Microdroplets," *Proceedings of the National Academy of Sciences* 115, no. 36 (September 2018): 8919.

87. M. Beyramali Kivy and M. Asle Zaeem, "Generalized Stacking Fault Energies, Ductilities, and Twinnabilities of CoCrFeNi-Based Face-Centered Cubic High Entropy Alloys," *Scripta Materialia* 139 (October 2017): 83.

88. S. Zhao, G. Ran, F. Li, H. Deng, and F. Gao, "Ab Initio Study of Interstitial Helium Clusters in 3C-SiC," *Journal of Nuclear Materials* 521 (August 2019): 13.